Rapidly convergent cluster expansion and application to lithium ion battery materials

Eunseok Lee,[1,*] Hakim Iddir,[2] and Roy Benedek[3]

[1]*Department of Mechanical and Aerospace Engineering, University of Alabama in Huntsville, Huntsville, Alabama 35899, USA*

[2]*Materials Science Division, Argonne National Laboratory, Argonne, Illinois 60439, USA*

[3]*Chemical Sciences and Engineering Division, Argonne National Laboratory, Argonne, Illinois 60439, USA*

(Received 16 October 2016; revised manuscript received 22 January 2017; published 22 February 2017)

The convergence of a cluster expansion for lithium transition-metal (TM) oxides is improved by explicit treatment of TM magnetic moments. The approach is applied to layered $LiCo_yNi_{1-y}O_2$ (NC). The ground state and low-lying excited state structures are identified, and the distribution of TM ions and magnetic moment in those structures is investigated to explain the origin of Ni-antisite ions and Jahn-Teller distortion. The developed model also reveals the mechanisms governing the atomic arrangement of NC, including in-plane Co-Co vs Co-Ni competition, magnetic frustration vs disproportionation competition, and cationic interactions spanning adjacent layers.

DOI: 10.1103/PhysRevB.95.085134

I. INTRODUCTION

Developing a cathode with high capacity and long lifetime is essential for the advancement of Li-ion battery technologies and relevant applications such as full-battery electric vehicles, portable electronic devices, smart grid systems, etc. The highest energy-density cathode materials are based on transition-metal (TM) oxides, such as $LiMO_2$ (M = Co, Ni, Mn) [1–4]. In particular, $LiNiO_2$ has received attention as a lower cost and toxicity alternative to the widely commercialized material $LiCoO_2$ [5–8]. However, the capacity fade with cycling has discouraged commercialization of $LiNiO_2$.

(Co,Al)-doped $LiNiO_2$, $LiNi_{1-y-z}Co_yAl_zO_2$ (NCA), was found to improve cycling performance [9–11], and capacities of 150–200 mAh/g have been demonstrated. For example, Jo *et al.* reported NCA delivered ∼155 mAh/g even at a 10 °C rate and after a capacity of 122 mAh/g was retained after 200 cycles [10]. However, the mechanism of the improved electrochemical performance remains to be clarified, which has slowed further development of Ni-based cathode materials. For example, the origin and role of Ni-Li exchange (to create Ni-Li antisite pairs), as well as the effects of Co and Al in NCA, are not fully understood [2,12–15]. Moreover, experiment has not confirmed the theoretically predicted Jahn-Teller (JT) distortion in the (rhombohedral) $LiNiO_2$ [7,14,16–19]. Thus, it would also be helpful to clarify the influence of Ni-antisite ions on the JT distortion.

One key to understanding these mechanisms is the relationship between atomic arrangement and thermodynamic properties; however, the atomic arrangement alone provides an incomplete description of TM oxides unless the magnetic degrees of freedom are accounted for [20,21].

In this paper, we apply the cluster expansion (CE) method to model the thermodynamic energy of fully lithiated $LiNi_{1-y}Co_yO_2$(NC), which may be viewed as a precursor to NCA. The ideal crystal structure of NC belongs to the $R\bar{3}m$ space group, with alternating layers of Li and TM ions, as illustrated in Fig. 1 [7,16–18,22]. To accommodate the atomic degrees of freedom of this system efficiently, we devise a generalized CE that includes the magnetic degrees of freedom explicitly. In particular, we design the expansion basis as a function of the coupled configuration of atom and magnetic moment, which enables us to elucidate the effects of magnetic interactions on the structural stability of NC, in particular regard to Ni-antisite ions and the JT distortion. Using the developed model, the role of Co substitution is also elucidated.

II. THE CE

The CE method enables calculation of configurational energy E for an arbitrary arrangement of atoms on a lattice from a set of effective cluster interactions (ECI), which are obtained by fits to the density functional theory (DFT) total energy calculations [23–25]. In the conventional CE, which we summarize briefly, the configurational energy of a system of N lattice sites occupied by m atomic species is expressed as an expansion [23,24]:

$$E(\{\sigma_i\}) = \sum_{(I)} V^{(I)}\Phi^{(I)}(\{\sigma_i\}), \tag{1}$$

where the discrete occupation variable σ_i indicates the atomic species at lattice site i. The compound index $I = I_1 I_2 \cdots I_N$ represents a permutation of m atomic species that occupy a set of N lattice sites; a given CE coefficient $V^{(I)}$ applies to all symmetrically equivalent (by translation and rotation) lattice-site clusters. The $\{I_i\}$ are numerically represented by integers $\{0, \ldots, m-1\}$, to map onto the chosen basis set described below. The functions of the occupation variables $\{\sigma_i\}$, $\Phi^{(I)}$, called cluster functions, are defined as $\Phi^{(I)} = \psi_{I_1}(\sigma_1)\psi_{I_2}(\sigma_2)\cdots\psi_{I_N}(\sigma_N)$, where $\psi_{I_i}(\sigma_i)$ is I_ith member of a complete basis set, such as the Chebyshev polynomials, adopted in this paper. As all the geometrically identical clusters have the same ECI, and by adopting $\psi_0(\sigma_i) = 1$, the expansion simplifies to

$$E(\{\sigma_i\}) = \sum_{\alpha}\sum_{(I')} V_\alpha^{(I')}\Phi_\alpha^{(I')}(\{\sigma_{i'}\}), \tag{2}$$

where α specifies each geometrically distinct cluster, $I' = I_1 I_2 \cdots I_{N_\alpha}$ is a length N_α permutation with repetition of $1,2,\ldots,m-1$; N_α is the size, and $\{\sigma_{i'}\}$ are the occupation variables of the lattice sites belonging to the cluster α. The coefficients $V_\alpha^{(I')}$ are obtained by fitting to data generated from DFT calculations. At each iteration step, (1) a CE model is constructed from DFT calculations for the current set of

*Corresponding author: eunseok.lee@uah.edu

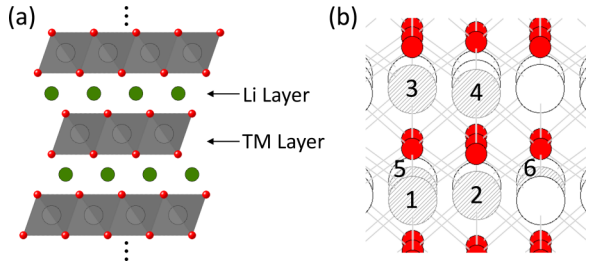

FIG. 1. Illustration of (a) the layered $LiMO_2$ crystal and (b) cationic lattice sites, indexed to specify the geometry of clusters corresponding to the selected cluster functions in Table I.

training configurations, (2) additional atomic configurations are generated to augment the training dataset, (3) DFT calculations are performed for the new configurations, and then (4) these new DFT calculations are added to the training data sets to construct a new tentative CE model in the next step, unless the discrepancy between the CE model prediction and DFT calculations is less than the selected criterion. Details of the fitting-prediction iteration are given in Refs. [23–26].

In principle, the completeness of the basis set Φ guarantees that the expansion can be made as precise as the DFT calculations from which the expansion coefficients $V_\alpha^{(I')}$ are derived, with the inclusion of a sufficiently large number of clusters. The precision and consistency for a given CE can be judged from the cross-validation (CV) score [23,26,27]. An explicit representation of the CV score in the leave-p-out ($1po$) scheme [28] is provided in the Supplemental Material S1 [29].

In practice, the computational burden required to obtain a precise set of coefficients $V_\alpha^{(I')}$ has imposed severe restrictions. The number of different atomic species has been restricted primarily to binary systems, with only a few existing applications of ternary systems [24,30,31] and quaternary systems [32] up to now, as the myriad DFT calculations required to achieve satisfactory results for larger site multiplicities has discouraged attempts to go beyond the ternary case. Computational constraints also limit maximum cluster sizes. To further reduce the computational burden, the cluster functions that have negligible ECI are also truncated through the fitting-prediction iteration.

III. APPLICATION TO NC

For the material of interest in the present paper, NC, the conventional choice for the site multiplicity, would be the ternary system with $m = 3$, i.e., Ni, Li, or Co. In the case of the cathode material LiFePO4, a two-sublattice CE was performed in which a binary formulation of the electronic degree of freedom on the Fe sublattice provided a satisfactory description [33]. In the system addressed in the present paper, the presence of both atomic and electronic degrees of freedom on the same sublattice make this a particularly challenging problem; the ions of Ni and Co have nonunique oxidation states Ni^{2+}, Ni^{3+}, Ni^{4+}, Co^{3+}, and Co^{4+}, as well as diverse spin states. In principle, a CE that did not explicitly include the electronic degrees of freedom but employed a sufficiently large set of cluster functions would implicitly take these internal atomic degrees of freedom into account. In practice, however, the convergence would likely be very slow.

We note that a full specification of the electronic degrees of freedom of atom $\sigma_{i'}$ would include both the oxidation state Z_i and the spin state s_i. In most instances, however, only a single relevant Z_i corresponds to a given s_i. For illustration, therefore, we introduce an approach in which the configuration specifies not only the atomic species (Li, Ni, Co) but also their most relevant spin states s_i (n spin states) for ions with a magnetic moment; the expansion could easily be generalized to include Z_i as well. Accordingly, the cluster function $\Phi_\alpha^{(I')}(\sigma_{i'})$ is generalized to the product $\Phi_\alpha^{(I'_A,I'_B)}(\sigma_{i'},s_{i'}) = \phi_\alpha^{(I'_A)}(\sigma_{i'})\phi_\alpha^{(I'_B)}(s_{i'})$ of atomic and spin functions. Correspondingly, the energy is expressed as

$$E(\{\sigma_i,s_i\}) = \sum_\alpha \sum_{(I'_A,I'_B)} V_\alpha^{(I'_A,I'_B)} \phi_\alpha^{(I'_A)}(\{\sigma_{i'}\})\phi_\alpha^{(I'_B)}(\{s_{i'}\}), \quad (3)$$

where the compound indices I'_A and I'_B are length N_α permutations with repetition of $1,2,\ldots,m-1$ and $1,2,\ldots,n-1$, respectively. An explicit representation of the cluster functions [24] is provided in the Supplemental Material S2 [29]. Compared to a treatment based on the conventional CE, Eq. (2), Eq. (3) includes an additional degree of freedom to account for the spin state; however, the additional complexity is more than offset by a reduction in the number of cluster functions necessary to obtain an acceptable CV score, and the resultant overall computational burden is greatly reduced. Furthermore, the present approach explicitly treats ferromagnetic vs antiferromagnetic coupling. We refer to the present treatment as a *spin-atom* CE to distinguish it from the conventional CE.

In the present treatment, therefore, a TM ion occupant of lattice site i is specified by its spin state, in addition to its atomic species σ_i. Thus, in the case of Ni^{3+} and Co^{4+}, s_i is a spinor with states $\pm\frac{1}{2}$, while it is 0 for Co^{3+} and Ni^{4+}. The space of spin states is larger than three, e.g., for Ni^{2+}; however, for computational convenience, we restrict the maximum number of spin states to three ($\pm\frac{1}{2}$ and 0) in this paper. As usual, the validity of the selected spin-atom CE scheme was tested, a posteriori, by the resultant CV score.

Evaluation of the contribution to Eq. (3) from a given atomic cluster α requires knowledge of the spin states $s_{i'}$. In practice, the CE coefficients V_α are fitted to DFT calculations at the generalized gradient approximation (GGA)+U level. Unfortunately, the precise spin states $s_{i'}$ are sometimes ambiguous in such calculations. This ambiguity was resolved in our paper with the help of Heyd-Scuseria-Ernzerhof hybrid-functional (HSE) [34,35], calculations, which provide more reliable values of $s_{i'}$ [31,34,36–38]. More specifically, additional HSE calculations with a hybrid functional separation parameter of 0.25 were performed for the same atomic configurations as used in GGA+U calculations on all two formula unit (f.u.) cells ($Li_2Ni_{2-y}Co_yO_4$) and a few larger cells (including $Li_6Ni_6O_{12}$, $Li_6Ni_4Co_2O_{12}$, $Li_{12}Ni_8Co_4O_{24}$, $Li_{16}Ni_8Co_8O_{32}$, and $Li_{40}Ni_{32}Co_8O_{40}$), and the resultant physically accurate magnetic moments were mapped onto the ones obtained at the GGA+U level. While the magnetic moment of Li was calculated to be nearly zero by both GGA+U and HSE in every examined case, discrepancies between GGA+U and

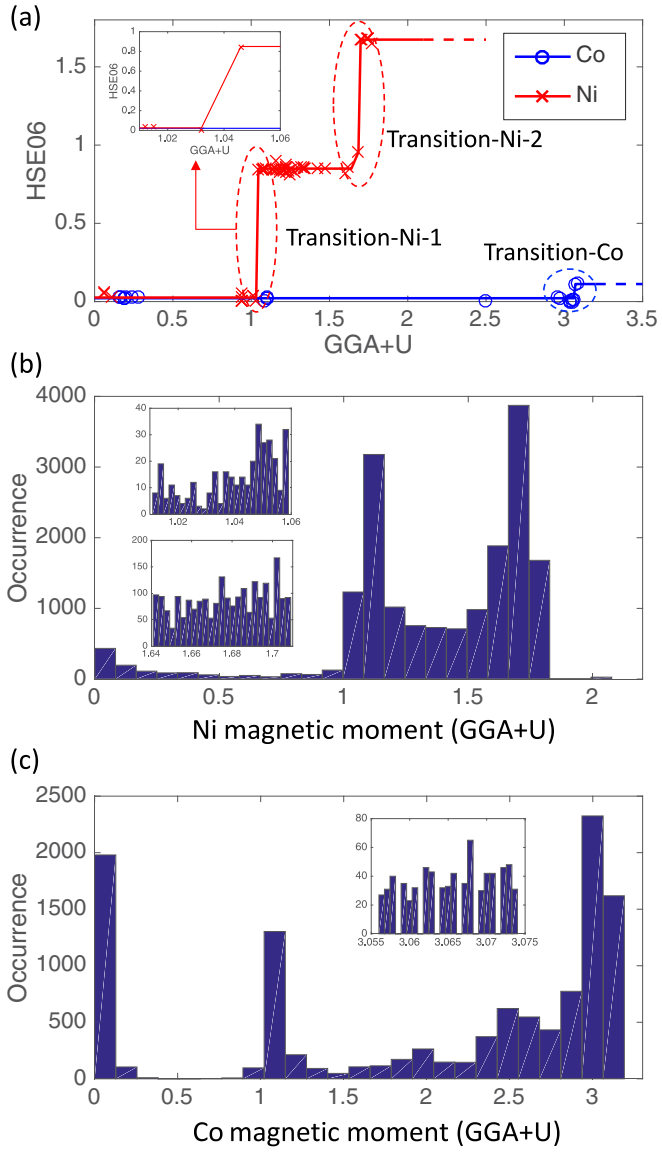

FIG. 2. (a) Comparison between the magnetic moment calculated by GGA+U to the one by hybrid DFT (HSE06 functional) performed on the same atomic configurations (unit: μ_B), (b) the frequency of occurrence of Ni's magnetic moment by GGA+U, and (c) the frequency of occurrence of the Co's magnetic moment by GGA+U. The histograms in (b) and (c) demonstrate that the occurrence of the magnetic moment by GGA+U in the transition ranges is substantial. Plateaus in (a) were obtained by taking averages locally. Inset figures in (a) are the zoom-in of $1.01 < m_{\mathrm{GGA}+U} < 1.06$ to show an example transition range for Ni more clearly. Note that the transition range for Co turns out to be ineffective later, as the converged CE selects $m_{\mathrm{Co}} = 3.072\mu_B$ such that all Co ions are nonmagnetic (see Supplemental Material S3 [29]). Inset figures in (b) and (c) are to demonstrate that the frequency of the occurrence in the transition ranges are substantial.

HSE were observed for magnetic moments of Co and Ni. Figure 2(a) illustrates the observed correspondence between the magnetic moment at the GGA+U level ($m_{\mathrm{GGA}+U}$) and the one at the HSE level (m_{HSE}). It is seen that for Co, $0 \sim 3.061\mu_B$ of $m_{\mathrm{GGA}+U}$ is mapped to zero of m_{HSE} and that $m_{\mathrm{GGA+U}} \geqslant 3.071\mu_B$ is mapped to $0.022\mu_B$ of m_{HSE}. $m_{\mathrm{GGA}+U}$ for Ni also has a wide range of values and is mapped to one of three values (0.026, 0.850, or $1.647\mu_B$) of m_{HSE}. Figures 2(b) and 2(c), which plot the histogram of $m_{\mathrm{GGA}+U}$ for Ni and Co, respectively, observed during the entire rounds of the iteration, demonstrate that $m_{\mathrm{GGA}+U}$ is also observed in the transition ranges occasionally. The lack of mapping data (GGA+U vs HSE) in these transition ranges hinders identifying the exact critical values of $m_{\mathrm{GGA}+U}$ at which the mapping of $m_{\mathrm{GGA}+U}$ to m_{HSE} changes. However, producing additional mapping data to obtain higher resolution transition ranges was not an efficient strategy due to orders of magnitude higher computational burden in hybrid DFT than nonhybrid DFT. Instead, we incorporate an additional degree of freedom m_M ($M =$ Li, Ni, Co) into CE and introduce a function $s_{i'}(m_{i'}, m_M)$. Here $s_{i'}$ is a discrete spin value, to be determined from the GGA+U calculated magnetic moment $m_{i'}$, which is effectively a continuous variable; when $m_{i'}$ is lower than m_M, $s_{i'}$ assumes one value, and when $m_{i'}$ is higher than m_M, $s_{i'}$ assumes a different value. Equation (3) is rewritten, to reflect that s_i is determined as a function of m_i and m_M, and the value of each m_M is also optimized (within the transition range) during the fitting-prediction iteration:

$$E(\{\sigma_i, s_i\}) = \sum_{\alpha} \sum_{(I'_A, I'_B)} V_{\alpha}^{(I'_A, I'_B)} \phi_{\alpha}^{(I'_A)}(\{\sigma_{i'}\}) \times \phi_{\alpha}^{(I'_B)}(\{s_{i'}(m_{i'}, m_M)\}). \quad (4)$$

A set of DFT calculations for individual atomic arrangements is performed to train the spin-atom CE given by Eq. (4). The GGA is applied with the Perdew-Burke-Ernzerhof parametrization [39,40], as implemented in VASP [41–43]. The (GGA)+U scheme was employed to account for the electron localization in TM oxides [44–46]. U values of 3.4 and 6.0 were chosen for Co and Ni ions, respectively [45–47]. A cutoff energy of 520 eV was used, and the k-point mesh was adjusted to ensure convergence of 1 meV per atom. The volume and shape of the supercell were allowed to change during the relaxation. The fitting-prediction iteration starts from small cells with high symmetry to decrease computational expense. During the subsequent iterations, supercells of increasing size were considered to enable treatment of greater disorder. To make precise comparisons between supercells of different size, the GGA+U was performed on a few high symmetry configurations for those supercells to ensure the converged energy per f.u. is independent of the supercell size.

IV. RESULTS

The ECI are obtained by the iterative process outlined in Sec. II. At each iteration step, fitting was made for a different number of cluster functions and different assumed values of m_M (within transition ranges), and the one providing the lowest CV score was selected to predict the new lowest energy configurations. It is convenient to employ the formation energy, $E_f(\mathrm{LiNi}_{1-y}\mathrm{Co}_y\mathrm{O}_2) = E(\mathrm{LiNi}_{1-y}\mathrm{Co}_y\mathrm{O}_2) - (1-y)\,E(\mathrm{LiNiO}_2) - yE(\mathrm{LiCoO}_2)$, as the fitted property so that the monomer term ($N_\alpha = 1$) in the CE vanishes. The E_f of all the configurations that were examined throughout the iteration is displayed in Fig. 3(a). For a detailed description of the convergence during the iteration, refer to Supplemental

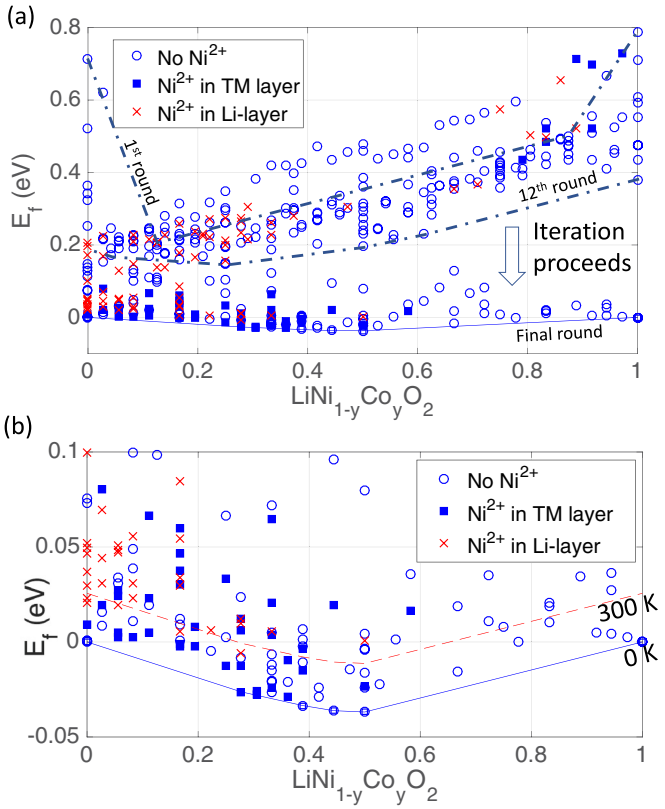

FIG. 3. Display of the E_f for the examined configurations during (a) the entire fitting-prediction iteration and (b) zoom-in view near the convex hull. (a) The continuous line indicates the convex hull on the converged iteration, while the dotted lines indicate the convex hulls using the newly predicted lowest energy configurations at the first and 12th rounds. (b) The continuous line and the dashed line indicate the convex hull at 0 K and its shift to 300 K (for comparison), respectively.

Material S3 [29]. The converged (spin-atom) CE model based on 396 GGA+U calculations consisted of 15 cluster functions (without counting the monomer) and yielded a CV score (by loo scheme) of 10.599 meV per f.u. and a mean-squared-error (mse) of 9.512 meV per f.u. in the prediction on the formation energy, an acceptable level of precision given the accuracy of the underlying DFT calculations. The CV score and mse as a function of the number of cluster functions, displayed in Fig. 4, show that the selected cluster functions are reliable. The CV scores by other 1po schemes for the selected cluster functions were similar to the one by loo; 10.608 meV (l2o), 10.617 meV (l3o), 10.624 meV (l4o), and 10.635 meV (l5o). The consistent CV scores in different 1po schemes also provide evidence of the reliability of the selected cluster functions. The spin state predicted by the converged CE agreed well with that obtained from DFT calculations, which provides additional evidence of convergence. For comparison, the most optimized (conventional) CE that were performed separately yielded a CV score of 32.067 meV per f.u., with 23 cluster functions. This result demonstrates the significance of the coupling between atomic and magnetic configurations and suggests that the spin-atom CE provides a more efficient basis than the conventional CE for insulating TM oxides. The selected cluster functions and the corresponding ECIs are

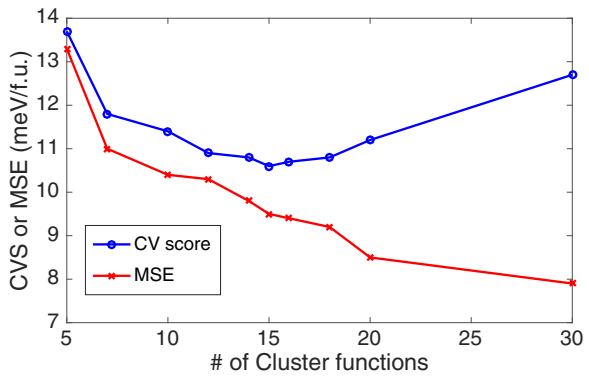

FIG. 4. The leave-one-out CV score and mean-squared-error as a function of the number of cluster functions at the last round of the fitting-prediction iteration. It is seen that the mse continues to decrease with the number of cluster functions, while the CV score rebounds when the number of cluster functions is more than 15.

listed in Table I, with illustration of the corresponding cationic sites in Fig. 1(b). Each ECI can quantitatively demonstrate the competing that determine atomic arrangements. For example, the value of $\Phi_{(2)}$ indicates that the nearest neighbor of Co-(magnetic)Ni pairs are more favorable than Co-Co pairs, while Co-(nonmagnetic)Ni pairs are less favorable. Large ECI values for three-body cluster functions imply that pairwise-only atomic interactions would fail to describe the thermodynamics of NC accurately.

From the convex hull of the formation energy, four ground states (stable states at 0 K), $LiNi_{0.72}Co_{0.28}O_2$, $LiNi_{0.61}Co_{0.39}O_2$, $LiNi_{0.66}Co_{0.44}O_2$, and $LiNi_{0.5}Co_{0.5}O_2$, between the two end states, $LiNiO_2$ and $LiCoO_2$, are identified. The atomic configurations of these ground states are presented in the Supplemental Material S4 [29]. The ground state $LiNi_{0.72}Co_{0.28}O_2$ contains Ni^{2+}, which indicates that the two two-phase regions, one between $y = 0$ and 0.28 and another between $y = 0.28$ and 0.39, contain Ni^{2+} in TM layers at 0 K, while in other ranges of y, the ground state contains

TABLE I. The selected cluster functions and corresponding ECIs (in eV). The lattice of the corresponding cations are indicated in Fig. 1.

$\Phi_{(n)}$	Cations	I'_A	I'_B	ECI
1	Empty			0.2538/f.u.
2	1, 2	22	22	0.0057
3	1, 4	12	12	0.0319
4	1, 4	22	12	−0.0136
5	1, 5	11	11	−0.0029
6	1, 5	22	11	0.0094
7	1, 5	22	22	−0.0044
8	1, 2, 3	222	222	0.0082
9	1, 2, 4	112	112	0.0028
10	1, 2, 4	222	122	−0.0092
11	1, 2, 5	222	111	0.0079
12	1, 2, 5	222	222	−0.0050
13	1, 2, 6	111	122	−0.0031
14	1, 2, 6	122	112	−0.0045
15	1, 2, 6	122	222	−0.0065

Ni^{3+} only. In addition to the ground states configurations, many low-lying excited states that are accessible by thermal fluctuation at low finite temperatures are observed throughout the compositional range, especially at the Ni-rich end. This suggests solid-solution behavior of NC (at finite temperature) at the Ni-rich end, but with short range order reminiscent of the ground state compounds at proximal compositions. Material properties at finite temperature should be determined not only by the ground states at 0 K but also the low-lying excited states. Many of these low-lying excited states contain Ni^{2+} in the TM layer as well as Ni-antisite ions. Although only a limited number of configurations were examined in the fitting-prediction iteration, the frequency of the appearance of Ni^{2+} in low-lying excited states is greatest at low y. Each data point displayed in Fig. 3 indicates only the presence of Ni^{2+} ions, not their concentration. We performed Monte Carlo simulations on a 4320 cationic lattice sites system (2160 f.u.) at 600 K (under the Curie temperatures for Ni and Co). The predicted equilibrium Ni-antisite concentration was 8.3 $\sim$ 11% for $y < 0.28$, but it suddenly decreased to 2.8% $\sim$ 3.9% in $0.28 \leqslant y \leqslant 0.5$ and nearly 0 in $y > 0.5$. These concentrations are compatible with the antisite disorder of a few percent, predicted in previous DFT calculations for pure $LiNiO_2$ [13,48,49]. This result also matches well to experimental data, which shows a high density of Ni-antisite ions at low y [3,14–16]. In the delithiated state, a fraction of cationic sites in the Li layer are vacant, and mobile Ni^{2+} in the TM layer will then tend to migrate to the vacant sites [50]. Hence, Ni-antisite concentrations will be even higher during charge-discharge cycling than in the pristine material.

We also calculated Ni-O bond lengths in the ground and low-lying excited states to investigate the JT distortion. The results show an attenuated JT distortion in the presence of either Ni^{2+} or Co substitution. For example, in the ground state at $y = 0$, each octahedral Ni had two 2.14 Å and four 1.91 Å Ni-O pairs, while in the next lowest energy state that contains 33% Ni^{2+} (among Ni ions), it had two 2.08 Å and four 1.97 Å Ni-O pairs, which implies partial removal of the JT distortion. Furthermore, the ground state at $y = 0.5$ had six 2.09 Å Ni-O pairs per each Ni, indicating total removal of the JT distortion. This result is consistent with the absence of any observed JT distortion in stoichiometric $LiNiO_2$ [16,17], including the bond lengths determined by NMR measurement [19], in contradiction to DFT calculations [7,14,18]. According to the results of this paper, Ni^{2+} is actively created at finite temperature and suppresses the JT distortion, which explains its nonobservation in experiment.

It is demonstrated that taking the magnetic configuration into account is critical for understanding the thermodynamics of NC. We find that only the Ni magnetic moments changed substantially with increasing y, which implies that Co remains trivalent over the entire compositional range. At $y = 0$, the ground state had the ideal layered structure of the $R\bar{3}m$ space group; all Ni ions are trivalent and reside in the TM layer, and the corresponding magnetic configuration exhibits the geometric frustration of antiferromagnetic (AFM) triangular lattices [cf. Fig. 5(a)], whereas the next lowest energy state at $y = 0$ contained Ni^{2+} and Ni^{4+} as a result of disproportionation: $2Ni^{3+} \rightarrow Ni^{2+} + Ni^{4+}$ [as illustrated in Fig. 5(b)], in which nearest-neighbor magnetic Ni ions (Ni^{2+} and Ni^{3+}) are antiferromagnetically paired, without frustration. Note that these two states have identical atomic arrangements but different thermodynamic energy due to distinct magnetic configurations. It might be expected that the presence of the unfavorable oxidation state Ni^{4+} would increase the thermodynamic energy significantly. However, the actual increase ($\Delta E_{\text{disprop}}$) is only 9.2 meV per f.u. because the energy increase from disproportionation is leveraged by removing the geometric frustration. The net effect of the lowered (electric charge state) symmetry and the removal of geometric frustration is a small but still positive $\Delta E_{\text{disprop}}$. On the other hand, (nonmagnetic) Co^{3+} substitutions can reduce the geometric frustration similarly to (nonmagnetic) Ni^{4+} but without either the disproportionation or the lowered symmetry. Co substitutions thus reduce the energy-above-hull of the low-lying excited states as well as decrease the number of Ni^{2+} in these low-lying excited states. The significance of interlayer interactions is also demonstrated by the present treatment. For example, the putative lowest energy state at $y = 1/3$ is a honeycomblike structure in which Co ions lie at the center of Ni hexagons so that Ni ions are antiferromagnetically paired. Despite its high symmetry and absence of the geometric frustration, this structure does not lie on the convex hull, which it would if only intralayer interactions were effective. Interlayer interactions are incorporated in the large ECI values of cluster functions $\Phi_{(3)}$, $\Phi_{(4)}$, $\Phi_{(8)}$, $\Phi_{(9)}$, and $\Phi_{(10)}$, which correspond to pair and three-body clusters that span adjacent TM and Li layers.

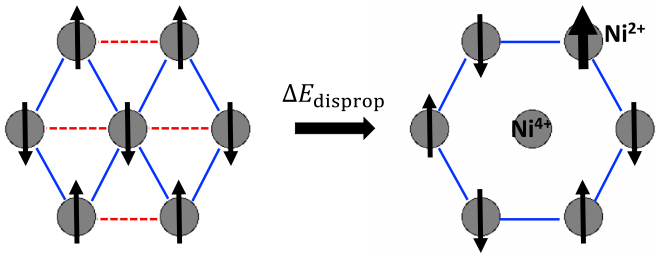

FIG. 5. Arrangement of magnetic moments in the TM layer of $LiNiO_2$: (a) ground state, (b) a low-lying excited state containing 33% Ni^{2+}. Gray circles indicate Ni^{3+} unless otherwise indicated, and arrows indicate the magnetic moment. Continuous and dashed lines indicate AFM and FM (magnetic) Ni-Ni pairs; geometric frustration of AFM ordering is observed in (a). The distribution of electric charge state will be more symmetric in (a) than (b). The displayed arrangements exist in the entire part, not the local part, of the material.

V. CONCLUSIONS

In summary, we modeled the thermodynamic energy of NC by a spin-atom CE, by which a satisfactory CV score was achieved with only a small set of clusters. This was accomplished by including the magnetic moment as well as the atomic species to identify the occupant of a given lattice site. It is observed that Ni^{2+} and Ni^{4+} (although unstable) can be created by the disproportionation of Ni^{3+}. The increase in energy is offset by removing the geometric frustration of AFM ordering. It was demonstrated that the competition of geometric frustration and disproportionation is critical in determining the atomic arrangement. The significance of interlayer cluster interactions and three-body cluster interactions

were also demonstrated quantitatively. It was seen that Co substitution provides a way to avoid the magnetic frustration more favorably than Ni disproportionation and reduce the Ni-antisite density. It was also shown that the JT distortion was suppressed by Ni^{2+} and Co. This approach can be extended to treat Ni-Mn-Co cathodes, as well as magnetic materials in general, such as spintronics materials.

ACKNOWLEDGMENTS

This research used resources of the National Energy Research Scientific Computing Center, which is supported by the Office of Science of the U.S. Department of Energy under Contract No. DE-AC02-05CH11231. The work at Argonne was performed under the auspices of UChicago Argonne, LLC, Operator of Argonne National Laboratory. Argonne, a U.S. Department of Energy Office of Science laboratory, which is operated under Contract No. DE-AC02-06CH11357. H.I. and R.B. acknowledge support from the Vehicle Technologies Office (VTO), Hybrid Electric Systems Program, David Howell (Manager), Battery R&D, Peter Faguy (Technology Manager), at the U.S. Department of Energy, Office of Energy Efficiency and Renewable Energy.

[1] P. Ramadass, B. Haran, R. White, and B. N. Popov, J. Power Sources **111**, 210 (2002).
[2] E. Zhecheva and R. Stoyanova, Solid State Ionics **66**, 143 (1993).
[3] M. Menetrier, A. Rougier, and C. Delmas, Solid State Commun. **90**, 439 (1994).
[4] R. Prasad, R. Benedek, and M. M. Thackeray, Phys. Rev. B **71**, 134111 (2005).
[5] T. Ohzuku, A. Ueda, and M. Nagayama, J. Electrochem. Soc. **140**, 1862 (1993).
[6] S. Yamada, M. Fujiwara, and M. Kanda, J. Power Sources **54**, 209 (1995).
[7] M. E. Arroyo y de Dompablo and G. Ceder, J. Power Sources **119–121**, 654 (2003).
[8] C. Delmas, J. P. Pérès, A. Rougier, A. Demourgues, F. Weill, A. Chadwick, M. Broussely, F. Perton, P. Biensan, and P. Willmann, J. Power Sources **68**, 120 (1997).
[9] F. Dogan, J. T. Vaughey, H. Iddir, and B. Key, ACS Appl. Mater. Interfaces **8**, 16708 (2016).
[10] M. Jo, M. Noh, P. Oh, Y. Kim, and J. Cho, Adv. Energy Mater. **4**, 1301583 (2014).
[11] F. Zhou, X. Zhao, and J. R. Dahn, J. Electrochem. Soc. **156**, A343 (2009).
[12] R. J. Clément, P. G. Bruce, and C. P. Grey, J. Electrochem. Soc. **162**, A2589 (2015).
[13] K. Hoang and M. D. Johannes, J. Mater. Chem. A **2**, 5224 (2014).
[14] H. Chen, J. A. Dawson, and J. H. Harding, J. Mater. Chem. A **2**, 7988 (2014).
[15] E. Zhecheva, R. Stoyanova, R. Alcántara, P. Lavela, and J.-L. Tirado, Pure Appl. Chem. **74**, 1885 (2002).
[16] A. Rougier, C. Delmas, and A. V. Chadwick, Solid State Commun. **94**, 123 (1995).
[17] I. Nakai, K. Takahashi, Y. Shiraishi, T. Nakagome, and F. Nishikawa, J. Solid State Chem. **140**, 145 (1998).
[18] H. Chen, C. L. Freeman, and J. H. Harding, Phys. Rev. B **84**, 085108 (2011).
[19] D. S. Middlemiss, A. J. Ilott, R. J. Clément, F. C. Strobridge, and C. P. Grey, Chem. Mater. **25**, 1723 (2013).
[20] J. B. Goodenough, Phys. Rev. **100**, 564 (1955).
[21] C. Zener, Phys. Rev. **82**, 403 (1951).
[22] P. Kalyani and N. Kalaiselvi, Sci. Technol. Adv. Mater. **6**, 689 (2005).
[23] J. M. Sanchez and D. de Fontaine, Phys. Rev. B **17**, 2926 (1978).
[24] C. Wolverton and D. de Fontaine, Phys. Rev. B **49**, 8627 (1994).
[25] A. Van der Ven, H.-C. Yu, G. Ceder, and K. Thornton, Prog. Mater. Sci. **55**, 61 (2010).
[26] A. Van der Ven, G. Ceder, M. Asta, and P. Tepesch, Phys. Rev. B **64**, 184307 (2001).
[27] P. D. Tepesch, M. Asta, and G. Ceder, Model. Simul. Mater. Sci. Eng. **6**, 787 (1998).
[28] I. V. Ozerov, E. D. Balitskaya, and R. G. Efremov, in *System-Specific Scoring Functions: Application to Guanine-Containing Ligands and Thrombin* (Springer, Netherlands, 2012), pp. 21–37.
[29] See Supplemental Material at http://link.aps.org/supplemental/10.1103/PhysRevB.95.085134 for definition of the cross-validation score, an explicit representation of cluster functions, description on the fitting-predicting iteration, and illustration of atomic arrangement of ground states (at $0K$).
[30] Y. S. Meng and M. E. Arroyo-de Dompablo, Energy Environ. Sci. **2**, 589 (2009).
[31] E. Lee and K. A. Persson, Adv. Energy Mater. **4**, 1400498 (2014).
[32] X. Huang, Z. Zhao, L. Cao, Y. Chen, E. Zhu, Z. Lin, M. Li, A. Yan, A. Zettl, Y. M. Wang, X. Duan, T. Mueller, and Y. Huang, Science **348**, 1230 (2015).
[33] F. Zhou, T. Maxisch, and G. Ceder, Phys. Rev. Lett. **97**, 155704 (2006).
[34] J. Heyd, G. E. Scuseria, and M. Ernzerhof, J. Chem. Phys. **118**, 8207 (2003).
[35] J. Heyd and G. E. Scuseria, J. Chem. Phys. **121**, 1187 (2004).
[36] J. Paier, M. Marsman, K. Hummer, G. Kresse, I. C. Gerber, and J. G. Angyán, J. Chem. Phys. **124**, (2006).
[37] J. Heyd, G. E. Scuseria, and M. Ernzerhof, J. Chem. Phys. **124**, 219906 (2006).
[38] H. Iddir and R. Benedek, Chem. Mater. **26**, 2407 (2014).
[39] J. P. Perdew, M. Ernzerhof, and K. Burke, J. Chem. Phys. **105**, 9982 (1996).
[40] J. P. Perdew, K. Burke, and M. Ernzerhof, Phys. Rev. Lett. **78**, 1396 (1997).
[41] G. Kresse and J. Hafner, Phys. Rev. B **47**, 558 (1993).
[42] G. Kresse and J. Furthmüller, Phys. Rev. B **54**, 11169 (1996).
[43] G. Kresse and J. Hafner, Phys. Rev. B **49**, 14251 (1994).
[44] A. I. Liechtenstein, V. I. Anisimov, and J. Zaanen, Phys. Rev. B **52**, R5467 (1995).
[45] L. Wang, T. Maxisch, and G. Ceder, Phys. Rev. B **73**, 195107 (2006).
[46] F. Zhou, M. Cococcioni, C. A. Marianetti, D. Morgan, and G. Ceder, Phys. Rev. B **70**, 235121 (2004).
[47] A. Jain, S. P. Ong, G. Hautier, W. Chen, W. D. Richards, S. Dacek, S. Cholia, D. Gunter, D. Skinner, G. Ceder, and K. A. Persson, APL Mater. **1**, 11002 (2013).
[48] K. Hoang and M. Johannes, Chem. Mater. **28**, 1325 (2016).
[49] Y. Kim, J. Phys. Chem. C **120**, 4173 (2016).
[50] J. Reed and G. Ceder, Chem. Rev. **104**, 4513 (2004).